Vision-Based Autonomous Steering of a Miniature Eversion Growing Robot

Zicong Wu, *Graduate Student Member, IEEE*, S. M. Hadi Sadati, *Member, IEEE*, Kawal Rhode, and Christos Bergeles, *Senior Member, IEEE*

***Abstract*—This letter presents vision-based autonomous navigation of a steerable soft growing robot. Our experimental platform is the previously presented MAMMOBOT, which is a small-diameter eversion growing robot with an embedded steerable catheter. The current manuscript first models the robot using kinematics (constant curvature) and mechanics (virtual work). Modelling considers the potential misalignment between the everting sheath and the embedded catheter. Second, a switching control architecture is proposed, wherein a model-based controller is employed for rapid convergence to a target position, followed by a closed-loop proportional controller that minimises the system's steady-state error. Feedback is visually provided from a calibrated stereo vision system. Target-positioning and trajectory-tracking experiments are conducted to evaluate the performance of the control architecture. Experimental results demonstrate the superiority of the mechanics-based modelling and control approach, showing an average accuracy of 0.67 mm (0.66% arclength) in target positioning experiments, and an accuracy of 0.72 mm (1.11% arclength) and 0.72 mm (1.01% arclength) for tracking a square trajectory and a circular trajectory, respectively. The autonomous steering framework is showcased within a 3D-printed mammary duct phantom. This work sets the stage for endoscope-based autonomous navigation of MAMMOBOT and similar soft growing steerable robots.**

***Index Terms*—Modeling, control and learning for soft robots, soft robot applications.**

I. Introduction

EVERSION growing robots extend their body by eversion of a folded internal structure at their tip, driven by hydraulic or pneumatic pressure [1], [2], mimicking "growing" of plants. Eversion robots can be steered actively, for example with tendons, or passively, by their environment-specific design and exploitation of interactions with it. Due to the growing robots' non-translational growth, they are favored for navigation in confined and fragile spaces, like rescue [3], exploration [4], and surgery [5].

Manuscript received 9 June 2023; accepted 26 September 2023. Date of publication 4 October 2023; date of current version 17 October 2023. This letter was recommended for publication by Associate Editor M. Wehner and Editor Y.-L. Park upon evaluation of the reviewers' comments. The work of Zicong Wu was supported by China Scholarship Council under Grant 202008060101. This work was supported in part by the Wellcome/EPSRC Centre for Medical Engineering under Grant WT203148/Z/16/Z and in part by the Innovate U.K. under the Horizon Europe Guarantee Extension under Grant 10062486. *(Corresponding author: Zicong Wu.)*

The authors are with the School of Biomedical Engineering and Imaging Sciences, King's College London, WC2R 2LS London, U.K. (e-mail: zicong.wu@kcl.ac.uk; m.hadi.sadati@gmail.com; kawal.rhode@kcl.ac.uk; christos.bergeles@kcl.ac.uk).

This letter has supplementary downloadable material available at https://doi.org/10.1109/LRA.2023.3322091, provided by the authors.

Digital Object Identifier 10.1109/LRA.2023.3322091

Modelling of soft growing eversion robots is a prerequisite for their control and autonomous deployment. In [6], quasi-static models were developed for the growing, retraction, and interaction of a proposed eversion vine robot. A nonlinear model predictive control scheme employed the kinematic model to monitor the growing process in [7]. Similarly, a quasi-static model integrated with a kinematic model to achieve tip positioning while taking loading and stiffness into account was developed in [8]. An interaction model accounting for collisions was proposed to support open-loop navigation in [9]. In [10], reduced-order modelling was introduced to capture growing robot dynamics. Cosserat rod [11] and physics-based finite element [12] models were investigated as geometrically accurate models for such robots. Energy shaping was also proposed for eversion control of a growing robot by considering the state of the ideal gas that is for actuation [13].

Among the modelling approaches described above, deriving the equation of motion based on the Principle of Virtual work is advantageous for modelling a soft robot due to the simplicity of incorporating different elements. As a result, this method is extensively utilized for trajectory optimization [14], bio-inspired design [15], control [16] and modelling the material non-linearity [17] of soft robots.

This letter presents modelling, control, and autonomous steering of a steerable everting robot termed MAMMOBOT [10], [12]. Both kinematics (constant curvature) and mechanics (virtual work) approaches are employed to implement the modelling of the eversion robot. Experiments are conducted to tune and investigate the effectiveness of the proposed models. Finally, a model-based controller using stereo vision tracking as position feedback is developed and evaluated within a control framework for autonomous steering of the robot. Target-approaching and trajectory-following experiments are carried out to evaluate the performance of the proposed controller and autonomous steering framework. Section II-A introduces our setup with its working principle. Modelling approaches and control architecture are detailed in Section II. Experimental setup and protocols are described in Section III. The experimental results and discussion, including evaluation and tuning of models, low-level duty cycle control, and autonomous steering, are found in Section IV. The manuscript concludes in Section V.

II. System Mechanics & Controller Design

MAMMOBOT, shown in Fig. 1, is developed for detection of abnormalities within the mammary ducts of the breast before they become apparent in mammography [10], [12]. The robot will endoscopically explore the mammary ducts, while in situ optical histopathology will classify the observed tissue [18].

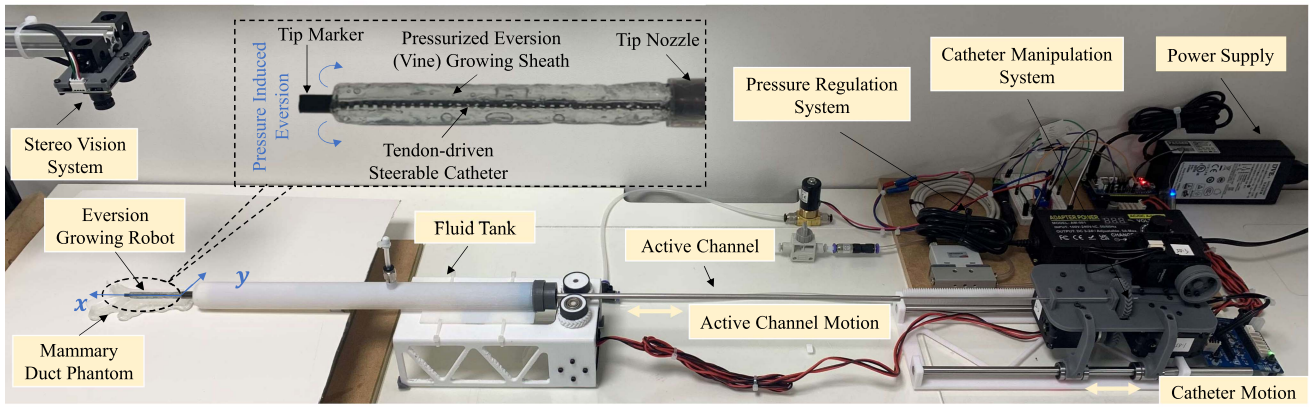

Fig. 1. MAMMOBOT setup with calibrated stereo vision system. The pressure regulation subsystem consists of an integrated electronic proportional micro regulator and a pneumatic solenoid valve for rapid response with high accuracy. An enlarged sub-figure demonstrates the details of the eversion growing tip.

Conventional fibreoptic ductoscopy [19] is not sufficiently flexible or steerable to solve this challenge. The sliding insertion of an endoscope [20] creates inevitable frictional forces against fragile mammary duct tissue and has no steerability. Eversion growing robots, on the other hand, showcase no sliding friction between the robot and the anatomy, making them ideal candidates.

TABLE I
ROBOT MODELING PARAMETERS

E_t^* [MPa]	E_c^* [MPa]	EI_c^* [Nm^2]	t [mm]
3	60	3.4254e-04	0.52
r_c [mm]	r_s [mm]	r_t [mm]	r_o [mm]
0.6	2.5	0.125	0.035

*Experimentally identified parameters.

A. Robot Architecture

Our robot architecture is separated into two sub-systems: 1) subsystem for manipulation of the eversion growing sheath, and 2) subsystem for manipulation of a steerable catheter. The steerable catheter reorients the growing sheath, which everts along the catheter-dictated trajectory.

As demonstrated in Fig. 1, the first subsystem comprises a growing eversion sheath embedded in a pressurised fluid-filled chamber, and an active channel for regulating the growing and retraction of the sheath alongside pressure control within the chamber. The second subsystem comprises a tendon-driven steerable catheter, fabricated by patterning NiTi tubing; a NiTi tendon to drive its deflection; a torque transmission shaft that passes through the active channel, fluid tank and growing eversion sheath, to enable the rotation of steerable catheter.

The sheath extends via tip eversion, i.e. rolling out, induced by its internal fluid pressure. The fluid tank is filled with saline and provides the necessary hydraulic pressure. The pressure is controlled via a low-level duty cycle controller that is detailed in Section III-D. The active channel is connected to the growing sheath to regulate its growth and retraction via a sliding motion. The catheter deflects under the pulling force of the internal tendon, and acts as the steerable backbone of the growing eversion robot.

B. Modelling Assumptions

To precisely control the robot tip, the relationship between the tendon displacement, inner pressure, robot length and catheter's shape should be modelled. Two different modelling approaches are presented and compared: inverse kinematics based on constant curvature, and mechanics modelling with the principle of virtual work.

In what follows, the catheter's lateral stiffness is assumed to be uniform along the robot length and of constant curvature when deflected. This assumption is in accordance with experimental observations. Several constant parameters appearing in the models can be retrieved from the manufacturer's data-sheets, e.g. the material properties of the catheter. The remaining parameters can be experimentally identified. All parameters appearing in the models presented in the following sections are shown in Table I.

In the following sections, five different models are demonstrated in total. **Kinematics model 1** is based on the assumption that the tendon is always aligned well with the catheter backbone; **Kinematics model 2** introduces the tendon offset to capture the practical behavior. **Mechanic model 1** is derived based on the principle of virtual work and **Mechanic model 2** is further improved by tuning of stiffness parameters, and **Mechanic model 3** is developed by taking the sheath-catheter misalignment into consideration.

C. Constant Curvature Kinematics

Fig. 2 shows the eversion growing robot deflected with a bending radius of R corresponding to a bending angle of θ, under the assumption of constant curvature. Assuming that the system's neutral axis with length l is on the catheter's concave surface, it can be easily determined that the bending radius is

$$\frac{R+r_c}{R} = \frac{l}{l_c} \rightarrow R = \frac{r_c l_c}{l - l_c}, \tag{1}$$

where r_c is the radius of steerable catheter, l_c is the catheter axial length, and l is the length of eversion growing robot. The simplest assumption is that the tendon remains along the catheter's central axis. Given the desired deflection radius, the tendon length l_t is given by **kinematics model 1**

$$l_t = l_c = lR/(r_c + R). \tag{2}$$

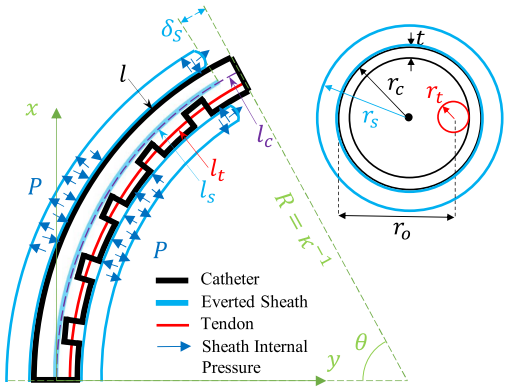

Fig. 2. Modeling diagram for the steerable catheter and eversion growing sheath. The coordinate frame is the same as the one in Fig. 1.

Kinematics model 1 assumes that the actuating tendon aligns well with the catheter's backbone, i.e. central axis, with known distal and proximal positions. In practice, however, the tendon will always deviate from the backbone, as demonstrated in Fig. 2. Therefore, the tendon offset r_o is introduced

$$r_o = 2r_c - 1.5t - r_t, \tag{3}$$

where r_t is the tendon radius, and t is the catheter thickness.

Then, **kinematics model 2** can be derived by substituting r_o for r_c in (1) and (2) as

$$R = \frac{\left(2r_c - \frac{3}{2}t - r_t\right) l_t}{l - l_t}, \tag{4}$$

$$l_t = \frac{lR}{\left(2r_c - \frac{3}{2}t - r_t\right) + R}. \tag{5}$$

Both kinematics models rely on the constant curvature assumption, which, even though widely used in modelling of continuum robots, may be violated in practice. Furthermore, (4)-(5) still assume that the tendon is a circular arc with fixed length and with its distal and proximal positions known. Finally, the tendon elastic elongation affects the deflection of the growing eversion robot.

To achieve modelling with higher fidelity, mechanics modelling based on the Principle of Virtual Work (PVW) is presented below.

D. Principle of Virtual Work Mechanics

The PVW method can be used to model the performance of soft robots and actuators. It derives the equilibrium equation of energy for a mechanical system by determining either the virtual force or virtual displacement.

Assuming that the eversion growing robot is deflected from its nominally straight shape when the tendon length changes from l to l_t, then the virtual work generated by the pressure inside the growing sheath W_p, steerable catheter bending W_c and tendon elongation W_t are

$$W_p = P \cdot V, \tag{6}$$

$$W_c = K_c\theta \cdot \theta, \tag{7}$$

$$W_t = K_t(l_t - l_{t0}) \cdot (l_t - l_{t0}), \tag{8}$$

where l_t and l_{t0} are the tendon deformed (elongated) and initial (after pulling by the actuation unit) length, P is the sheath internal relative pressure, $V = \pi r_s^2 l_c$ is the sheath volume, $\theta = l/(R + r_c)$ is the catheter bending angle, $K_c = E_c\pi(r_c^4 - r_i^4)/(4\,l)$ is the bending stiffness of the steerable catheter, $K_t = E_t\pi r_t^2/l_{t0}$ is the tensile stiffness of the tendon, and $r_i = r_c - t$ is the catheter inner radius.

The equilibrium equation for energy conversation holds as

$$\partial W_p + \partial W_c + \partial W_t = 0. \tag{9}$$

Each differential term can be expressed w.r.t. the system's kinematics states, i.e. current bending radius R as

$$\partial W_p = P\pi r_s^2 \cdot \partial l_c/\partial R, \tag{10}$$

$$\partial W_c = K_c\theta \cdot \partial\theta/\partial R = \frac{-K_c\theta l}{(R + r_c)^2}, \tag{11}$$

$$\partial W_t = K_t(l_t - l_{t0}) \cdot \partial l_t/\partial R, \tag{12}$$

where r_s is the sheath radius.

Then **mechanic model 1** can be developed as follows. Substituting (10)–(12) into (9), the deflection radius becomes

$$R = \frac{l_{t0}}{4r_c}\frac{E_c r_c^4 - 4Pr_c^2 r_s^2 + 4E_t r_c^2 r_t^2 - E_c r_i^4}{l_{t0}Pr_s^2 + E_t l r_t^2 - E_t l_{t0} r_t^2}. \tag{13}$$

In other words, the deflection radius of the eversion growing robot can be determined if the sheath pressure, everted length, and tendon length are provided.

Likewise, the desired tendon length can be determined from the expected deflection radius, as shown in (14), which forms the "inverse kinematics" of the eversion growing robot as

$$l_t = \frac{4E_t R l r_c r_t^2}{E_c\left(r_c^4 - r_i^4\right) - 4\left[r_c^2\left(Pr_s^2 - E_t r_t^2\right) - Rr_c\left(Pr_s^2 - E_t r_i^2\right)\right]}. \tag{14}$$

A more accurate model can be derived by using (5) for calculating l_t. Furthermore, the catheter elasticity can be calculated as $K_c = EI_c/l$ to account for the catheter cut pattern and PTFE tubing, where EI_c is an experimentally identified bending modulus for the combined system. The mechanics model can be updated as **mechanic model 2**

$$R = \frac{l_{t0}\left(-P\pi r_c^2 r_s^2 + E_t\pi r_c^2 r_t^2 + EI_c\right)}{r_c\pi\left(l_{t0}Pr_s^2 + E_t l r_t^2 - E_t l_{t0} r_t^2\right)}, \tag{15}$$

$$l_t = \left(E_t R l r_c r_t^2\pi\right) / \left(-P\pi r_c^2 r_s^2 + E_t\pi r_c^2 r_t^2 - RP\pi r_c r_s^2 + E_t R\pi r_c r_t^2 + EI_c\right). \tag{16}$$

E. Eversion Sheath-Catheter Misalignment

As the everting element elongates or retracts, the catheter's tip should remain aligned with it. Misaligned growth, however, is possible due to wrinkles in the sheath or sheath-catheter friction. Therefore, **mechanic model 3** is developed by taking the misalignment into consideration. This discrepancy, δ_s, between the sheath's endpoint and the catheter's length can be calculated through the sheath volume $V = \pi r_s^2 l_s$, where l_s is the sheath length, by updating (2) as $l_s = R(l - \delta_s)/(r_c + R)$.

Experimental observations confirmed that the change in the exposed catheter tip curvature is negligible and the Constant Curvature assumptions remain valid for the whole length of the robot. Further discussion is provided in the following sections.

F. Control Architecture

Considering 2D motion for simplicity, the system control input u is the catheter insertion displacement Δl and tendon pulling displacement Δl_{t0}, i.e. $u = [\Delta l, \Delta l_{t0}]$. A hybrid switching control architecture is proposed. The hybrid controller switches between an open-loop model-based controller and a closed-loop model-less proportional controller. The open-loop controller is activated for configurations that are not in the vicinity of the target tip position, which is determined through stereo vision. The closed-loop controller takes over in vicinity of the target to minimise the steady-state error.

The open-loop model-based controller relies on an inverse Constant Curvature model to calculate the robot's shape based on the current (x, y) and desired (x^*, y^*) tip position, as

$$R = \left(x^2 + y^2\right)/2x,\ l = 2R\,\mathrm{atan2}(y, x). \tag{17}$$

The configuration parameters for the robot's current shape, i.e., (l, R), are calculated based on the robot tip Cartesian position (x, y) that is measured via stereo vision tracking. The same holds for the robot target shape (l^*, R^*), which is calculated from the robot tip target position (x^*, y^*). The system input vector then becomes $u = [l^* - l, l^*_{t0} - l_{t0}]$. We observed that the model-based controller was successful in bringing the robot close to the target shape, but could not achieve zero steady state error due to the modelling uncertainties.

The closed-loop model-less proportional controller can then accommodate for the modelling uncertainties in the vicinity of the target position. In this case, the system inputs rely on the error between the system control inputs and the robot tip current and target positions according to

$$u = K_p \cdot [x^* - x, y^* - y]. \tag{18}$$

Controller switching is decided by comparing the error between the robot current and desired length $l^* - l$, as well as the tendon displacement error $l^*_{t0} - l_{t0}$, against a set of empirically determined threshold values (ϵ_l & ϵ_{t0}), as

$$u = \begin{cases} [l^* - l, l^*_{t0} - l_{t0}], & \text{if } l^* - l > \epsilon_l \\ & l^*_{t0} - l_{t0} > \epsilon_{t0}. \\ K_p \cdot [x^* - x, y^* - y], & \text{otherwise} \end{cases} \tag{19}$$

The system diagram is shown as **Controller** block in Fig. 3.

III. Experimental Setup & Procedures

This section provides details on the robot implementation and the visual system that provides control feedback.

A. Steerable Soft Growing Robot Structure

The growing eversion sheath is of 5.0 mm diameter and fabricated according to [10]. The steerable catheter fabricated by laser notch patterning on NiTi tubing is of 1.2 mm diameter, while the NiTi wire actuating it is of 0.25 mm diameter. Dynamixel MX-64 AR actuation units (Robotis Inc., USA) are in a daisy chain to drive the system's elements, interfacing with the Dynamixel OpenCM 9.04 C controller (Robotis Inc., USA) and Dynamixel 485 expansion board (Robotis Inc., USA) for communication and powering.

To avoid sudden rupture induced by excessive pressure, the hydraulic pressurization approach in [10] was replaced by pneumatic pressurization with air-water interfacing. In this way, the pressure in the fluid tank can be precisely tuned while maintaining a high-speed response. A K8P electronic proportional micro regulator (Camozzi Automation S.p.A., Italy) connected to compressed air (pressure of 4.0 bar) is employed for pressure regulation. It works jointly with an SVQ three-way pneumatic solenoid valve (SMC Corporation, USA) for rapid air release. Both components are controlled by an analog signal from the OpenCM 9.04 C controller to achieve the desired pressure within the pressurisation chamber. A pair of BT-210 BlueTooth communication modules are integrated as well. The follower module is interacting with the Dynamixel controller via serial communication (UART), while the leader module is mounted onto the RC-100B device as a remote controller. This enables tele-operative control to offer flexibility to robot manipulation.

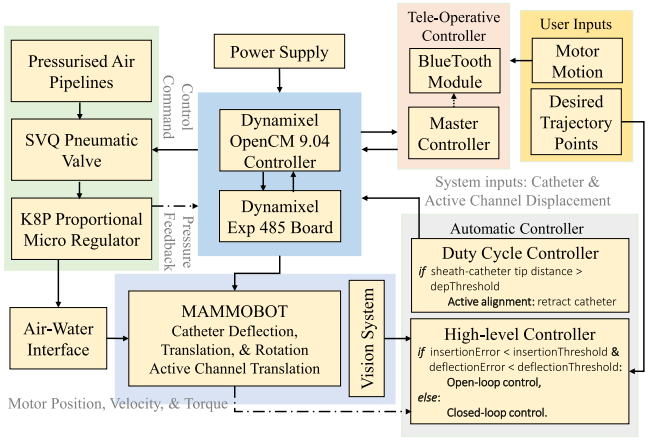

Fig. 3. MAMMOBOT system diagram for autonomous navigation and tele-operative control. Solid lines stand for **commands**, while dashed lines for **feedback**. The **Controller** block shows the switching control architecture.

The robot is tested in a workspace similar to a sphere sector with a radius of 100 mm, i.e. the robot's maximum length, and an opening angle of about 65°.

B. Visual Tracking System

The clinical manifestation of our system will employ and thin fibre optics endoscope housed within its lumen. An alternative exploration will consider real-time fluoroscopic guidance, similar to mammographic CT, for real-time localisation based on our prior work [21]. Both of these cases are considered vision-based tracking, which is the only realistic option given that the small dimensions of the robot preclude the use of electromagnetic trackers. As a result, the control scheme is proposed based on stereo visual tracking. We are obviating the computer vision challenges by using a stereo vision system with direct line of sight. The controller operates using measurements in the coordinate frame of the tracking system, i.e. measured by the stereo vision tracking system, rather than the global (robot) frame. This strategy can compensate for the associated visual tracking errors. The employed tracking system architecture and its accuracy are presented below.

A stereo vision system is established using two high-resolution USB webcams (EPL, China) with a high frame rate of 120 fps and a resolution of 1280 × 720. The vision system was calibrated using the *stereoCameraCalibrator* toolbox of MATLAB, and a checkerboard with a total size of 100 × 70 mm

and individual square size of 10×10 mm. Up to 18 frames at different positions and orientations were collected to calibrate the tracking system. The mean overall re-projection error after calibration was 0.29 pixels.

To evaluate the vision tracking system accuracy, an electromagnetic (EM) reference disc (Northern Digital Inc, USA), which also acted as a visual marker, was sequentially placed at 20 locations to cover the observable workspace of the stereo rig. The marker was simultaneously identified in both the vision and EM tracking systems. Stereo reconstruction via triangulation provided the 3D locations of the marker, which was subsequently compared with the coordinates returned by a registered NDI Aurora EM tracking system (Northern Digital Inc, USA). The mean square root error between the data from both systems was 1.26 mm. This error demonstrates the importance of defining the target position in the vision tracking system's frame rather than the robot's global frame.

C. Alignment Based on Individual Robot Component Tracking

A marker made of black heat-shrinkable tubing covered the exterior of the catheter's tip, so that it could be reliably detected and tracked by simple brightness thresholding of the video streams in real-time. The centroid of the detected pixels was then used to triangulate the tip's 3D coordinates. These coordinates were then registered to the robot's coordinate frame and broadcasted to the robot controller. The robot and the stereo vision coordinate frames were calibrated via manual measurements and comparison of the Cartesian and pixel locations in the tracking space. Individual tracking of growing sheath was developed in a similar vein to allow for the active alignment of the sheath tip and catheter tip. Once the length discrepancy between the two is found larger than an empirically defined threshold, the pressure regulating everting element growth is reduced, while the catheter is automatically retracted or inserted to re-establish alignment. Everting element tracking was achieved by using colour saline as the pressurisation medium; recall that the everting element is transparent. The effectiveness of active alignment is evaluated in both trajectory following experiments and phantom experiments via the average sheath-catheter tip distance, where the complicated robot configuration and environmental interaction pose the most challenges to alignment.

D. Low-Level Duty Cycle Control for Aligned Growing

Key to our robot's actuation is pressure regulation within the fluid tank and sheath to achieve growing and retraction. As explained in [10], low-level duty cycle control is required. High pressure is required to achieve eversion, while low pressure is required to enable catheter advancement and steering.

Fig. 4 demonstrates low-level duty cycle control in practice. During t_1, the inner pressure is regulated to high level with an absolute pressure of 135 kPa. In the meantime, the steerable catheter and active channel are translated in tandem. The forward motion of active channel releases the growing sheath while the forward motion of catheter helps eversion-based growing of sheath with friction force betwen them. This achieves growing via sheath eversion with pressure-induced torque. During t_2, inner pressure is released to a low level, i.e., 105 kPa, and the actuator motion is reversed to re-align the catheter with growing sheath. Both t_1 and t_2 are 1.0 s.

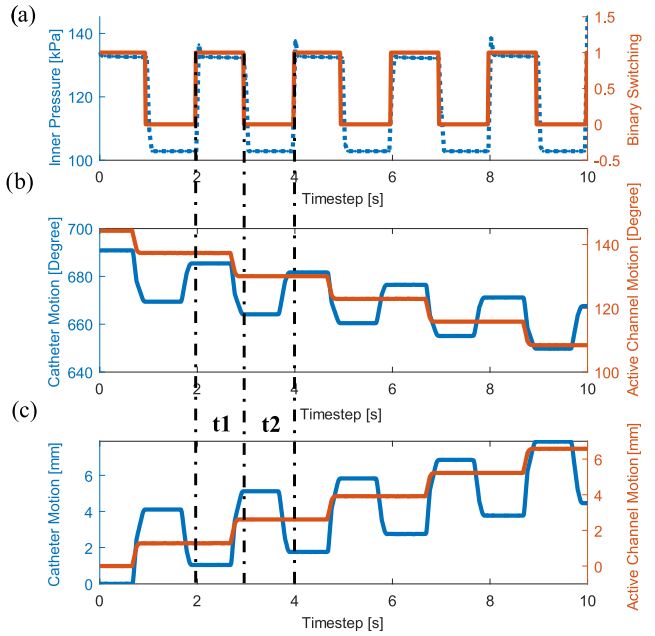

Fig. 4. Low-level duty cycle control for aligned translation of the catheter and growing sheath. a) Pressure regulation and periodic binary switching between low (0) and high (1) pressure levels. b) Periodic angular motion of actuators to drive the translation of catheter (blue) and active channel (red). c) Periodic translational motion of the catheter (blue) and the active channel (red).

The miniature design of the system means that such an iterative motion was needed to achieve growing and the catheter/everting element alignment. As a result, a zig-zag pattern is observed during the target and trajectory tasks. In our low level duty cycle controller, the corresponding actuator rotation steps for the insertion motion, retraction motion of catheter, and the feeding motion of the active channel are set as 20 deg, 15 deg, and 10 deg, respectively, to achieve a full growing cycle with improved alignment. The retraction cycle is implemented in the same way but with reversed direction.

E. Vision-Based Controller & Autonomous Steering

The controller continuously acquires frames incoming from the visual system to obtain the coordinates of the target position and current catheter tip position, and sheath tip position at each time point. First, the distance between catheter and sheath is computed; if the distance is larger than the threshold, set at 6 mm, the active alignment is activated to retain alignment. Otherwise, the error between the target position and tip position becomes the input to the model-based controller, which determines the desired motion for each actuator, i.e., *dynamixel_insert* and *dynamixel_deflect*.

The controller has three modes that are implemented until the system converges to the target position: 1) Insertion only, when *dynamixel_insert* is larger than *insertionThreshold*; 2) Deflection only, when *dynamixel_insert* is smaller than *insertionThreshold* but *dynamixel_deflect* is larger than *deflectionThreshold*; 3) when the current position of robot is close enough to target position, the closed-loop model-less proportional controller is activated. During the controller tuning, it was observed that when taking the robot tip distance to the target as a threshold to switch the controller mode, the converged position error was still

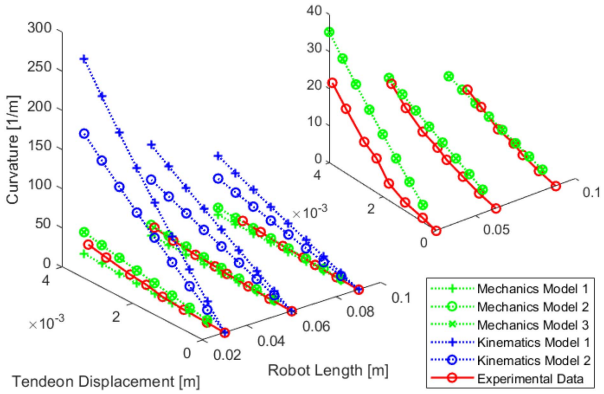

Fig. 5. Experimental evaluation of robot's curvature from kinematics and mechanics models with various robot lengths and tendon displacements. The sublet on the right-top corner compares the mechanics model 2 & 3, and experimental ground truth.

TABLE II
ERROR ANALYSIS FOR KINEMATICS AND MECHANICS MODELS

Model	Kinematic		Mechanic		
	#1	#2	#1	#2	#3
MAE $[m^{-1}]$	75.58	44.03	5.87	4.49	4.49

large (up to about 2 mm). Alternatively, a significantly smaller convergence error (up to 1 mm) was observed when considering the difference between the current actuator values with the inverse model predictions, i.e. the model-based controller output. The latter method was employed in our controller. In our experiments, the controller switching threshold values *insertionThreshold* and *deflectionThreshold* were set to $\epsilon_l = 5$ mm and $\epsilon_{t0} = 0.5$ mm, respectively. The proportional gain was set as 0.14. Trajectory autonomous steering was achieved by approximating the target trajectory as a series of target-positioning steps.

IV. EXPERIMENTAL RESULTS & DISCUSSIONS

Target-positioning and trajectory-following tasks are implemented with our robot setup to evaluate the performance of modelling and model-based controller. Target positioning experiments consist of 16 sets of individual tasks. In trajectory-following experiments, both square and circular trajectories are employed for further evaluation. Analysis of experimental results is provided in detail as well.

A. Parameter Tuning

Experimental evaluation and tuning are carried out to verify the performance of these models. For mechanics modelling, the mechanical properties of the growing eversion robot matters. Considering that the bending stiffness of the robot contributes the majority of modelling error, the parameter E_c, E_t, and EI_c are the first parameters to be tuned, as reported in Table I. Fig. 5 compares the experimental data with kinematics and mechanics modelling at sampled coordinates, both before and after tuning. Numerical results are also shown in Table II. It should be noticed that compared with **mechanics model 2**, **mechanics model 3** takes misalignment into account. Experimental results shows that the same MAE w.r.t. experimental ground truth reported from them, i.e., both are $4.49\,\mathrm{m}^{-1}$, which suggests a negligible effect from misalignment.

TABLE III
ERROR ANALYSIS FOR TARGET POSITIONING CONTROL PERFORMANCE

MAE [mm]	MAE [%Arc]	σ [mm]	σ [%Arc]	Norm. Err.
0.67	0.66%	0.20	0.58%	1.06%

TABLE IV
TRAJECTORY TRACKING ERROR ANALYSIS*

MAE [mm]	0.72 (1.11%)[1.99%]	0.72 (1.01%)[2.40%]
σ[mm]	0.24 (0.46%)[0.66%]	0.22 (0.37%)[0.73%]
Avg. Dep. [mm]	3.33	3.09
Max. Iter.	231	282
Completion Time [s]	603	425

*Euclidean distance error in the registered frame in mm (arclength normalized error %) [workspace diagonal normalized error %]

B. Target Positioning

16 target positions are defined and evenly distributed within the robot's workspace while being observable by the stereo camera rig. The points cover a grid of 60 mm × 20 mm. The robot is autonomously navigated to each target, always starting from its zero/retracted configuration. The mechanics model-based controller demonstrated an overall Euclidean distance error of 0.67 mm (0.66% normalized error w.r.t. the robot's current arclength, and 1.06% normalized error w.r.t. the robot's workspace diagonal) in the registered robot frame. It is observed that the closed-loop model-less proportional controller was always activated to fine-tune target reach. Result analysis is provided in Table III.

Fig. 6 demonstrates the real-time 2D position and Euclidean distance between the robot's current position and target position, using the proposed hybrid controller, i.e., the mechanics model-based controller with a closed-loop proportional controller. Positions in the X and Y axes are also plotted to visualize the approaching process. The convergence of the kinematics model-based controller is faster than the others, which can be explained by the relatively larger actuator motion determined by the kinematics model when given a desired configuration. However, it experienced more and larger oscillations during motion, especially when the robot was deflected. In contrast, the mechanics model-based controller demonstrates more stable performance in both directions. It converged, however, with an observable distance error, which suggests the necessity of fine-tuning with a closed-loop controller. It can be observed that the closed-loop proportional controller significantly reduced the distance error and outperformed the others. The final converged positions from our proposed mechanics model-based controller with closed-loop proportional tuning are plotted in Fig. 7.

C. Trajectory Tracking

Similarly, trajectory tracking is implemented with the proposed hybrid controller to further evaluate its performance. A square trajectory with a dimension of 30 mm × 20 mm, and a circular trajectory with a diameter of 30 mm, are introduced. Experimental results are demonstrated in both Table IV and Fig. 8. The reference trajectories are plotted with a red line while

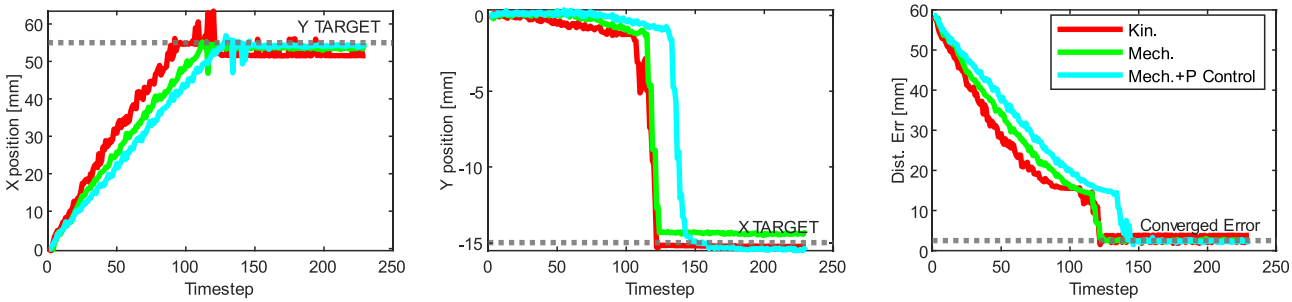

Fig. 6. Target positioning controller performance for the open-loop model-based controller and the switching closed-loop control scheme.

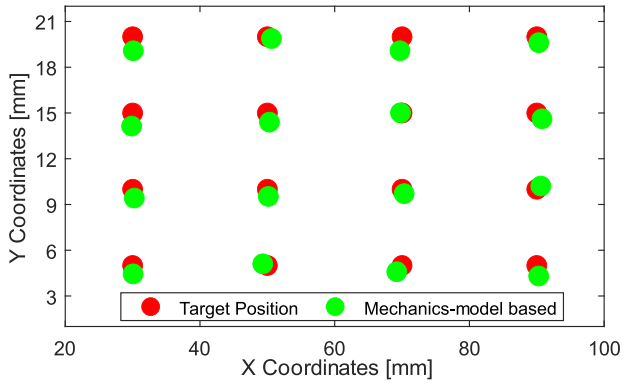

Fig. 7. Target positioning experiments. The ground truth is plotted in red while converged positions from the switching controller are plotted in green.

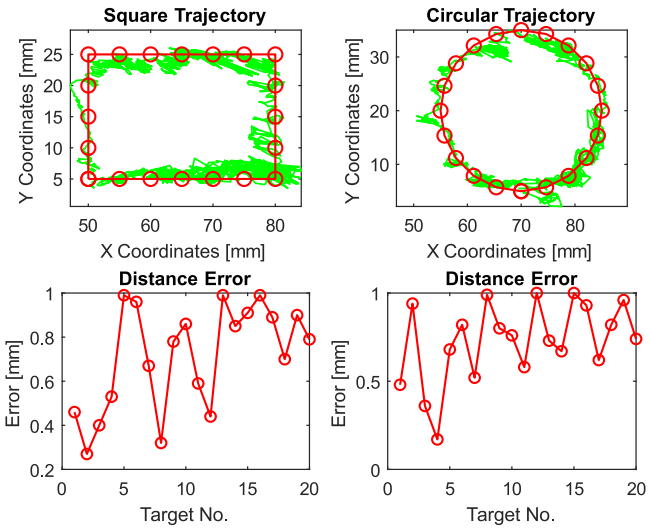

Fig. 8. Trajectory tracking performance of the switching controller. The ground truth is plotted in red while converged positions from the switching controller are plotted in green.

the robot trajectories are plotted in green. Reference targets and corresponding targets from real trajectories are marked with red circles, and red dots, respectively. The converged error at each target is also plotted. The MAE (Mean Absolute Error) for square trajectory and circular trajectory is 0.72 mm (1.11% arclength) and 0.72 mm (1.01% arclength), with a standard

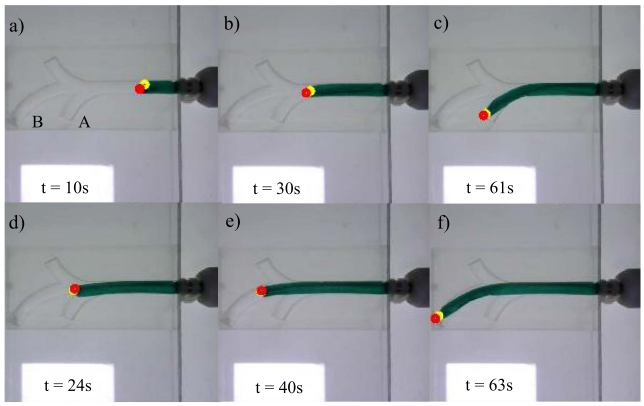

Fig. 9. Navigation performance of the proposed control architecture in a breast duct-like phantom: a-c) navigation in branch A and d-f) navigation in branch B. The red dot shows the tip of steerable catheter while the yellow dot is the tip of colored growing sheath.

variance of 0.24 mm (0.66% arclength) and 0.22 mm (0.37% arclength), respectively. Moreover, the normalized error using the workspace diagonal of both trajectories is 1.99% and 2.40%, separately. During both trajectory tracking experiments, the average distance between catheter and sheath tips is 3.33 mm and 3.09 mm, respectively, which is close to the catheter exterior length in each duty cycle and demonstrates the effectiveness of the proposed active alignment. The zig-zag pattern observed between the consecutive points is unavoidable due to the robot's low-level recursive actuation cycle as explained in Section III-D.

D. Phantom Navigation

A mammary duct-like phantom was fabricated by a Formlabs 3B SLA printer using Clear material (Formlabs Inc., US), based on the scaled-up (re-doubled) models reported in [10]. With the proposed model-based controller, the robot autonomously navigates to sub-branch A and B, shown as sequence a) to c) and d) to f) in Fig. 9, respectively. Fig. 10 demonstrates the real trajectories of the robot during navigation by both autonomous navigation and teleoperative control, which are plotted in blue, and green, separately. The reference trajectory points are plotted in red.

The zig-zag patterns are observed in both navigation modes, as previously explained. Even though experiments quantified the performance of our proposed model-based controller and image-based autonomous steering framework, it should be noted that: 1)

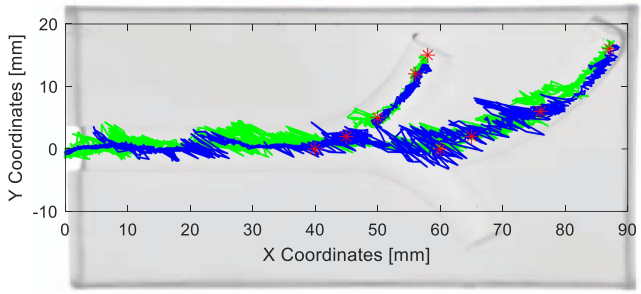

Fig. 10. Phantom navigation experimental results: autonomous steering control trajectories (blue), reference trajectory points (red), and the trajectories during manual teleoperation (green).

the current tracking method is easy to be affected by illumination conditions; 2) low-level control of the duty cycle cannot always perfectly align the growing sheath and the catheter, especially when the catheter is deflected; 3) trajectory sampling affects performance, i.e., relative denser targets are necessary to guide the robot to steer into the desired branch, limited by control mode detailed in Section III-E and the catheter's small inherent curvature, which should be taken into account during experiments. Autonomous navigation is significantly quicker than teleoperative control (124 s vs 235 s), highlighting the advantages of our proposed control architecture. Also, the average discrepancy between sheath and catheter tips during navigation is 3.45 mm.

V. Conclusion

In this letter, we developed and evaluated a kinematics and mechanics model for our steerable growing eversion robot, wherein steering is achieved by an inner-placed tendon-driven catheter. An autonomous steering framework was established with visual feedback from the calibrated stereo system, based on a mechanics model-based controller and a closed-loop model-less proportional controller. Active alignment between the catheter tip and sheath tip was developed as well based on individual tracking of the two. Adequate growth alignment between the catheter and the sheath has been achieved in both free space and phantom interaction. Issues were still present when passing high curvature bends, due to the environmental friction and imperfections in the robot fabrication.

The proposed control architecture was evaluated by target positioning, trajectory following, and phantom navigation experiments with a scaled-up mammary duct phantom.

Future work will integrate a miniature endoscope within the growing sheath for imaging acquisition during in-situ diagnosis and steering via on-board means, or external fluoroscopic approaches. By modelling the whole system and model-based parametric study as well as control optimization, catheter/sheath alignment and control performance can also be further improved.

Acknowledgments

For the purpose of open access, the author has applied for a CCBY licence to any Author Accepted Manuscript version arising from this submission.

References

[1] E. W. Hawkes, L. H. Blumenschein, J. D. Greer, and A. M. Okamura, "A soft robot that navigates its environment through growth," *Sci. Robot.*, vol. 2, no. 8, 2017, Art. no. eaan3028.
[2] S. K. Talas, B. A. Baydere, T. Altinsoy, C. Tutcu, and E. Samur, "Design and development of a growing pneumatic soft robot," *Soft Robot.*, vol. 7, no. 4, pp. 521–533, 2020.
[3] P. A. der Maur et al., "RoBoa: Construction and evaluation of a steerable vine robot for search and rescue applications," in *Proc. IEEE 4th Int. Conf. Soft Robot.*, 2021, pp. 15–20.
[4] P. Li, Y. Zhang, G. Zhang, D. Zhou, and L. Li, "A bioinspired soft robot combining the growth adaptability of vine plants with a coordinated control system," *Research*, vol. 2021, 2021, Art. no. 9843859.
[5] C. Simpson, B. Huerta, S. Sketch, M. Lansberg, E. Hawkes, and A. Okamura, "Upper extremity exomuscle for shoulder abduction support," *IEEE Trans. Med. Robot. Bionics*, vol. 2, no. 3, pp. 474–484, Aug. 2020.
[6] L. H. Blumenschein, M. M. Coad, D. A. Haggerty, A. M. Okamura, and E. W. Hawkes, "Design, modeling, control, and application of everting vine robots," *Front. Robot. AI*, vol. 7, 2020, Art. no. 548266.
[7] H. El-Hussieny, I. A. Hameed, and J.-H. Ryu, "Nonlinear model predictive growth control of a class of plant-inspired soft growing robots," *IEEE Access*, vol. 8, pp. 214495–214503, 2020.
[8] C. Tutcu, B. A. Baydere, S. K. Talas, and E. Samur, "Quasi-static modeling of a novel growing soft-continuum robot," *Int. J. Robot. Res.*, vol. 40, no. 1, pp. 86–98, 2021.
[9] D. A. Haggerty, N. D. Naclerio, and E. W. Hawkes, "Characterizing environmental interactions for soft growing robots," in *Proc. IEEE/RSJ Int. Conf. Intell. Robots Syst.*, 2019, pp. 3335–3342.
[10] P. Berthet-Rayne et al., "MAMMOBOT: A miniature steerable soft growing robot for early breast cancer detection," *IEEE Robot. Automat. Lett.*, vol. 6, no. 3, pp. 5056–5063, Jul. 2021.
[11] M. Selvaggio, L. A. Ramirez, N. D. Naclerio, B. Siciliano, and E. W. Hawkes, "An obstacle-interaction planning method for navigation of actuated vine robots," in *Proc. IEEE Int. Conf. Robot. Automat.*, 2020, pp. 3227–3233.
[12] Z. Wu et al., "Towards a physics-based model for steerable eversion growing robots," *IEEE Robot. Automat. Lett.*, vol. 8, no. 2, pp. 1005–1012, Feb. 2023.
[13] E. Franco, "Model based eversion control of soft growing robots with pneumatic actuation," *IEEE Control Syst. Lett.*, vol. 6, pp. 2689–2694, 2022.
[14] J. M. Bern, P. Banzet, R. Poranne, and S. Coros, "Trajectory optimization for cable-driven soft robot locomotion," *Robot.: Sci. Syst.*, vol. 1, no. 3, 2019.
[15] C. Ahn, X. Liang, and S. Cai, "Bioinspired design of light-powered crawling, squeezing, and jumping untethered soft robot," *Adv. Mater. Technol.*, vol. 4, no. 7, 2019, Art. no. 1900185.
[16] Y. Shengda, T. Wang, and S. Zhu, "Research on energy consumption of fiber-reinforced fluidic soft actuators," *Smart Mater. Structures*, vol. 30, no. 2, 2021, Art. no. 0 25036.
[17] F. Renda, C. Armanini, A. Mathew, and F. Boyer, "Geometrically-exact inverse kinematic control of soft manipulators with general threadlike actuators' routing," *IEEE Robot. Automat. Lett.*, vol. 7, no. 3, pp. 7311–7318, Jul. 2022.
[18] A. Ezzat et al., "Preliminary findings of confocal laser endomicroscopy and Raman spectroscopy in human breast tissue characterisation," *Eur. J. Surg. Oncol.*, vol. 48, no. 5, pp. e221–e222, 2022.
[19] K. Mokbel, P. F. Escobar, and T. Matsunaga, "Mammary ductoscopy: Current status and future prospects," *Eur. J. Surg. Oncol.*, vol. 31, no. 1, pp. 3–8, 2005.
[20] A. Dubowy, M. Raubach, T. Topalidis, T. Lange, S. Eulenstein, and M. Hünerbein, "Breast duct endoscopy: Ductoscopy from a diagnostic to an interventional procedure and its future perspective," *Acta Chirurgica Belgica*, vol. 111, no. 3, pp. 142–145, 2011.
[21] A. Vandini, C. Bergeles, B. Glocker, P. Giataganas, and G.-Z. Yang, "Unified tracking and shape estimation for concentric tube robots," *IEEE Trans. Robot.*, vol. 33, no. 4, pp. 901–915, Aug. 2017.